


Diffraction Phenomena in Time-Varying Metal-Based Metasurfaces

Antonio Alex-Amor^{1,*}, Salvador Moreno-Rodríguez,² Pablo Padilla², Juan F. Valenzuela-Valdés,² and Carlos Molero²

¹*Department of Information Technology, Universidad San Pablo—CEU, CEU Universities, Campus Montepríncipe, Boadilla del Monte (Madrid) 28668, Spain*

²*Department of Signal Theory, Telematics and Communications, Universidad de Granada, Granada 18071, Spain*

 (Received 28 July 2022; revised 16 December 2022; accepted 23 February 2023; published 5 April 2023)

This paper presents an analytical framework for the analysis of time-varying metal-based metamaterials. Specifically, we particularize the study to time-modulated metal-air interfaces embedded between two different semi-infinite media that are illuminated by monochromatic plane waves of frequency ω_0 . The formulation is based on a Floquet-Bloch modal expansion, which takes into account the time periodicity of the structure ($T_s = 2\pi/\omega_s$) and integral-equation techniques. It allows us to extract the reflection and transmission coefficients as well as to derive nontrivial features about the dynamic response and dispersion curves of time-modulated metal-based screens. In addition, the proposed formulation has an associated analytical equivalent circuit that gives a physical insight into the diffraction phenomenon. Similarities and differences between space- and time-modulated metamaterials are discussed via the proposed circuit model. Finally, some analytical results are presented to validate the present framework. Good agreement is observed with numerical computations provided by a self-implemented finite-difference time-domain (FDTD) method. Interestingly, the present results suggest that time-modulated metal-based screens can be used as pulsed sources (when $\omega_s \ll \omega_0$), beam formers ($\omega_s \sim \omega_0$) to redirect energy in specific regions of space, and analog samplers ($\omega_s \gg \omega_0$).

DOI: [10.1103/PhysRevApplied.19.044014](https://doi.org/10.1103/PhysRevApplied.19.044014)

I. INTRODUCTION

The propagation properties of electromagnetic waves through time-varying media constitute a topic that has classically been studied to understand effective modulations produced by the interaction of two waves [1,2]. In recent years, the topic has been revisited due to the potential applications of time-varying systems in communications. Exotic properties related to the inherent nonreciprocity [3,4] or beam-steering capabilities [5] have attracted the interest of many researchers. At the same time, the theoretical background associated with time-varying systems has benefited from fruitful development. This is the case for the generalization of the Kramer-Kronig relations to temporal scenarios [6], forms of dual behavior in spatially and temporally varying systems [7], or the discovery of promising scenarios based on moving gratings [8]. A complete compilation of space-time media is reported in Refs. [9,10], exposing the general concepts and examining the theoretical implications and promising fields of application.

Modern time-varying systems are based on periodic structure and metasurface configurations, the architecture of which can approximately be interpreted as periodic or quasiperiodic distributions of individual emitters or meta-atoms [11,12]. Following this line of argument, further definitions are discussed for temporal systems in Ref. [13]. An original concept arises by mixing classical metamaterials and metasurfaces with time modulation. The fundamental advantage of this concept is the long tradition of metamaterials and metasurfaces in the microwave and photonics communities and the vast knowledge accumulated recently from both the experimental and the manufacturing point of view [14–16]. Time modulation can individually be incorporated on meta-atoms by, among others, reconfigurable mechanical, electrical, or optical elements [17].

These spatiotemporal metamaterials and metasurfaces have succeeded in the realization of nonreciprocal systems. Nonreciprocity, in this context, occurs when the metastructure receives radiation from a given direction and reflects it along a second direction but the opposite situation does not take place. In other words, time-reversal symmetry is broken [18]. A plethora of works have been published remarking on this property [19,20]. Other works, such as Refs. [21,22], have benefited from this property

*Corresponding author. antonio.alexamor@ceu.es

in the course of deriving some applications. Some other applications use temporal systems to tailor the frequency modulation, such as those in Refs. [5,23,24] for wavefront control, in Ref. [25] for direction-of-arrival (DOE) estimation, or in Ref. [26] for multiplexing.

The analysis and design of temporal and spatiotemporal models is hindered by the lack of availability of commercial tools. Generally, a home-made numerical code based on the finite-difference time-domain (FDTD) method [27] provides a good physical insight, especially to simulate the time evolution of systems. However it is unable to provide specific parameters such as reflection and transmission coefficients and more refined techniques are commonly needed. For example, for time-varying dielectric slabs, Ref. [28] employs a classical mode-matching technique, whereas Ref. [29] solves the eigenvalue problem of the dispersion equation. A mode-matching technique is also applied in Ref. [3] for a space-time periodic grating. Some other techniques depart from a Floquet analysis, implementing the spatially-discrete traveling-wave (SD-TW) modulation [11] or modeling a Huygens metasurface with Lorentzian dispersion models [30]. In Ref. [31], the solution of the system is found due to the implementation of a method of moments (MoM). Circuit-model interpretations have also been reported based on shunt topologies derived from admittance matrices [32,33]. In most cases, direct comparisons with results provided by FDTD are needed to validate the models [34,35].

The state-of-the-art works in the literature have traditionally focused on the study of dielectriclike systems with spatiotemporal variation. This work discusses time-varying systems of a metallic nature, consisting of infinitely extended metallic screens that appear and vanish periodically. This situation emulates systems in the microwave, millimeter, and low-terahertz regions, where metals behave as good conductors. A plane wave impinges on the structure, interacting with the time-modulated screen. Despite the simplicity of the scenario, it is prone to posing problems in terms of a Floquet analysis and a subsequent circuit analysis. The derivation of simple expressions for the circuit elements allows the reader to acquire a substantial physical insight. The methodology is motivated by previous analysis reported in the literature, as in Refs. [36–38] for one-dimensional (1D) structures and Refs. [39–42] for two-dimensional (2D) structures modulated in space. The structure considered in this paper is a kind of analog but in time. The conclusions extracted from this work can easily be extended to other higher-dimensional structures modulated in both time and space.

The time-periodic system presented here is formed by a screen that periodically alternates between “metal” and “air” states. To recreate this system in a real-world implementation would require the use of materials, of a metallic and/or semiconductor nature, that can be electronically reconfigured. 2D materials such as graphene, molybdenum

disulfide (MoS₂) and hexagonal boron nitride (*h*-BN) could be an interesting option to consider [43–45]. For instance, it is well known that graphene can act as a metal (good conductor) when it is electrically biased. Moreover, the sheet resistance of graphene can be reconfigured depending on the bias [46–48]. Thus, graphene can act as a good conductor (metal state), as a bad conductor, as an absorber, and as a transparent layer that is perfectly matched to the surrounding media [49,50]. Transparentlike responses would lead to the realization of the air state. Naturally, a periodic tuning of the sheet resistance of the graphene to achieve metal and air states would require appropriate and specific control electronics. Alternatively, up to microwave frequencies, the use of conventional electronically reconfigurable schemes based on PIN and varactor diodes could be considered. To recreate “air” and “metal” states in our time-periodic system would require the realization of a reconfigurable planar frequency-selective surface (FSS). When properly designed, the reconfigurable FSS would allow full transmission (air state) and full reflection (metal state) of the incident electromagnetic waves [51]. In a metallic FSS, full transmission and reflection can be achieved by means of resonances in a particular range of frequencies.

The paper is organized as follows. Section II is devoted to the exposition of the theoretical background, analysis of the dynamic and dispersion response, and circuit derivation. In Sec. III, we evaluate and validate the proposal. The conclusions of the work are presented in Sec. IV.

II. THEORETICAL FORMALISM

The scenario to evaluate a time-varying metallic structure is depicted in Fig. 1. An infinitely extended time-varying interface is placed in between two semi-infinite media ($i = 1$ for input, $i = 2$ for output). The interface (or discontinuity) is a perfect-electric-conductor (PEC) sheet that appears and vanishes periodically with period T_s

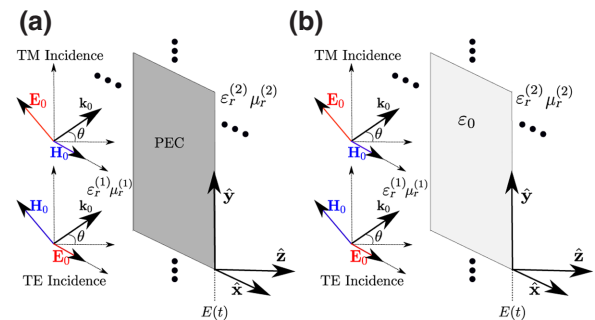


FIG. 1. A sketch of the scenario. The time interface is found at position $z = 0$. (a) The time interval when the interface is a PEC sheet (“metal” state). (b) The time interval when the interface vanishes (“air” state).

and angular frequency $\omega_s = 2\pi/T_s$. A plane wave vibrating with period of T_0 and angular frequency $\omega_0 = 2\pi/T_0$ illuminates the discontinuity. A real implementation of a system of this kind can be, for example, a graphene sheet switching between conductor and nonconductor states, controlled by an external bias voltage [46–48].

Let us define an arbitrary plane wave impinging on such a discontinuity. Assuming TE incidence, the fields associated with this plane wave are expressed as

$$\mathbf{E}_0 = e^{j\omega_0 t - jk_t y - j\beta_0^{(1)} z} \hat{\mathbf{x}}, \quad (1)$$

$$\mathbf{H}_0 = Y_0^{(1)} e^{j\omega_0 t - jk_t y - j\beta_0^{(1)} z} [\hat{\mathbf{y}} \cos(\theta) - \hat{\mathbf{z}} \sin(\theta)], \quad (2)$$

where we assume unit electric field amplitude. The parameter $Y_0^{(1)}$ is the wave admittance in the incidence region (1) ($z < 0$), and the vectors $k_t = \sqrt{\varepsilon_r^{(1)} \mu_r^{(1)}} k_0 \sin(\theta)$ and $\beta_0^{(1)} = \sqrt{\varepsilon_r^{(1)} \mu_r^{(1)}} k_0 \cos(\theta)$ refer to the transverse and longitudinal components of the incident wave vector, respectively. The angle θ corresponds to the incidence angle. In the case of TM incidence, the fields of the incident plane wave are expressed as

$$\mathbf{E}_0 = e^{j\omega_0 t - jk_t y - j\beta_0^{(1)} z} [\hat{\mathbf{y}} \cos(\theta) - \hat{\mathbf{z}} \sin(\theta)], \quad (3)$$

$$\mathbf{H}_0 = Y_0^{(1)} e^{j\omega_0 t - jk_t y - j\beta_0^{(1)} z} \hat{\mathbf{x}}. \quad (4)$$

A. Floquet-Bloch expansion

Due to the existence of the time-varying interface and its interaction with the incidence wave, the global transverse electromagnetic field in region (1) can be represented in terms of a Floquet series:

$$\begin{aligned} \mathbf{E}_t^{(1)}(y, z, t) = & \left[e^{j\omega_0 t - jk_t y - j\beta_0^{(1)} z} + R e^{j\omega_0 t - jk_t y + j\beta_0^{(1)} z} \right. \\ & \left. + \sum_{\forall n \neq 0} E_n^{(1)} e^{j\omega_n t - jk_t y + j\beta_n^{(1)} z} \right] \hat{\mathbf{x}}, \end{aligned} \quad (5)$$

$$\begin{aligned} \mathbf{H}_t^{(1)}(y, z, t) = & \left[Y_0^{(1)} e^{j\omega_0 t - jk_t y - j\beta_0^{(1)} z} - R Y_0^{(1)} e^{j\omega_0 t - jk_t y + j\beta_0^{(1)} z} \right. \\ & \left. - \sum_{\forall n \neq 0} Y_n^{(1)} E_n^{(1)} e^{j\omega_n t - jk_t y + j\beta_n^{(1)} z} \right] \hat{\mathbf{y}}, \end{aligned} \quad (6)$$

where $E_n^{(1)}$ is the amplitude of the n th harmonic, R is the reflection coefficient caused by the time-varying interface, and ω_n is the angular frequency associated with the n th-order harmonic:

$$\omega_n = \omega_0 + n\omega_s. \quad (7)$$

As can be appreciated in Eqs. (5)–(7), the Floquet harmonics include a dependence not only on the angular rate

of change ω_s , related to the time-varying metallic screen, but also on the angular frequency of the incident plane wave, ω_0 . The additional phase factor that ω_0 brings to the series suggests that the problem cannot be reduced to a conventional Fourier series.

In a similar way, we define the transverse electromagnetic field at the region (2) ($z > 0$),

$$\begin{aligned} \mathbf{E}_t^{(2)}(y, z, t) = & \left[T e^{j\omega_0 t - jk_t y - j\beta_0^{(2)} z} \right. \\ & \left. + \sum_{\forall n \neq 0} E_n^{(2)} e^{j\omega_n t - jk_t y - j\beta_n^{(2)} z} \right] \hat{\mathbf{x}}, \end{aligned} \quad (8)$$

$$\begin{aligned} \mathbf{H}_t^{(2)}(y, z, t) = & \left[T Y_0^{(2)} e^{j\omega_0 t - jk_t y - j\beta_0^{(2)} z} \right. \\ & \left. + \sum_{\forall n \neq 0} Y_n^{(2)} E_n^{(2)} e^{j\omega_n t - jk_t y - j\beta_n^{(2)} z} \right] \hat{\mathbf{y}}, \end{aligned} \quad (9)$$

where T denotes the transmission coefficient and $E_n^{(2)}$ is the amplitude associated with an n th-order Floquet harmonic.

In the former expressions, $Y_n^{(i)}$ is the admittance of the i th medium ($i = 1$ for input, $i = 2$ for output) associated with the n th-order harmonic:

$$Y_n^{(i)} = \frac{\varepsilon_r^{(i)} \varepsilon_0 \omega_n}{\beta_n^{(i)}}, \quad \text{TM incidence}, \quad (10)$$

$$Y_n^{(i)} = \frac{\beta_n^{(i)}}{\mu_r^{(i)} \mu_0 \omega_n}, \quad \text{TE incidence}, \quad (11)$$

with

$$\beta_n^{(i)} = \sqrt{\left[k_n^{(i)} \right]^2 - k_t^2}, \quad (12)$$

$$k_n^{(i)} = \sqrt{\varepsilon_r^{(i)} \mu_r^{(i)}} \frac{\omega_n}{c}. \quad (13)$$

The parameter $k_n^{(i)}$ is the n th-order wave number and $\beta_n^{(i)}$ its corresponding propagation constant, both in region (i). For TE incidence, just TE admittances in Eq. (11) take part in Eqs. (6) and (9). Similarly, for TM incidence, Eqs. (6) and (9) use TM admittances only.

B. Dispersion properties

Figure 2 illustrates the dispersion relation $\omega(k)$ for the time-modulated metallic screen. The dispersion curves are linear (nondispersive) for all the considered harmonics n and are separated from each other by ω_s . Moreover, no stop-band region is observed. This is due to the infinitesimal thickness of the time-modulated screen. Actually, this situation is expected to hold as long as the thickness of the screen is much smaller compared to the incident wavelength. This is a remarkable difference compared to

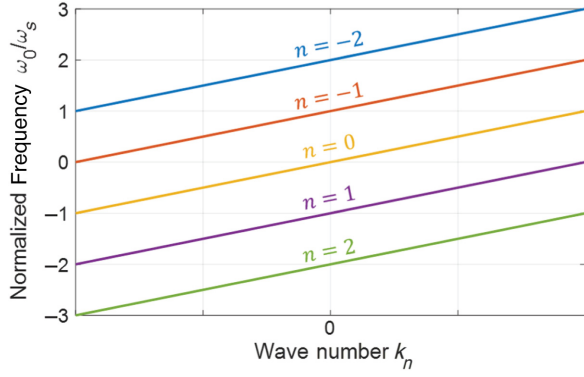


FIG. 2. The dispersion curves for the time-modulated metallic screen.

time-modulated dielectric slabs $\varepsilon(t)$ [28,29], which are typically dispersive and present forbidden bands. Another fact to note is the existence of negative frequencies and wave numbers. This means that the corresponding n th-order wave number is negative, referring to a mode traveling backward [3].

Additionally, by looking at Eqs. (12) and (13), it can be readily inferred that most of the diffraction orders created by time-varying metallic screen are purely propagative. It can be demonstrated that only a few negative integer orders n are evanescent (β_n should be imaginary for evanescent waves). These orders would be restricted to

$$-\frac{\omega_0}{\omega_s} [1 + \sin(\theta)] < n < -\frac{\omega_0}{\omega_s} [1 - \sin(\theta)], \text{ eva. waves,} \quad (14)$$

when the considered background is air. In fact, in case of normal incidence ($\theta = 0$), there are no evanescent waves. Conversely, larger ω_0/ω_s ratios in combination with large incident angles θ suggest that a greater number of modes are evanescent.

C. Time-varying E field at the discontinuity: Equivalent-circuit interpretation

In order to proceed, we assume *a priori* knowledge of the time-dependent field profile at the discontinuity. Without loss of generality, it can be described by a function depending on time, $\mathbf{E}(t)$. This assumption allows us to apply and adapt the models presented in Refs. [36,37] for a time-periodic problem.

Thus, we begin by imposing the continuity of the electric field at the interface $z = 0$,

$$\mathbf{E}^{(1)}(y, 0, t) = \mathbf{E}^{(2)}(y, 0, t) = \mathbf{E}(t), \quad (15)$$

where both $\mathbf{E}^{(1)}(y, 0, t)$ and $\mathbf{E}^{(2)}(y, 0, t)$ have their field profile at the discontinuity $\mathbf{E}(t)$. This equality allows us to

apply standard Fourier analysis, through which we reach the following expressions:

$$(1 + R) = T = \frac{1}{T_s} \int_{-T_s/2}^{T_s/2} E(t) e^{-j\omega_0 t} dt, \quad (16)$$

$$E_n^{(1)} = E_n^{(2)} = \frac{1}{T_s} \int_{-T_s/2}^{T_s/2} E(t) e^{-j\omega_n t} dt. \quad (17)$$

From Eqs. (16) and (17), we obtain the following relationship:

$$E_n^{(1)} = E_n^{(2)} = (1 + R)N(\omega_n), \quad (18)$$

where

$$N(\omega_n) = \frac{\int_{-T_s/2}^{T_s/2} E(t) e^{-j\omega_n t} dt}{\int_{-T_s/2}^{T_s/2} E(t) e^{-j\omega_0 t} dt} \quad (19)$$

accounts for the coupling between the incident wave and the corresponding n th-order harmonic.

Now, the continuity of the instantaneous Poynting vector at the interface is imposed. The power passing through the interface is evaluated over a period T_s ,

$$\int_{-T_s/2}^{T_s/2} \mathbf{E}(t) \times \mathbf{H}^{(1)}(y, 0, t) dt = \int_{-T_s/2}^{T_s/2} \mathbf{E}(t) \times \mathbf{H}^{(2)}(y, 0, t) dt, \quad (20)$$

leading to

$$\begin{aligned} (1 - R)Y_0^{(1)} \int_{-T_s/2}^{T_s/2} E(t) e^{j\omega_0 t} dt \\ - (1 + R) \sum_{\forall n \neq 0} N(\omega_n) Y_n^{(1)} \int_{-T_s/2}^{T_s/2} E(t) e^{j\omega_n t} dt \\ = (1 + R)Y_0^{(2)} \int_{-T_s/2}^{T_s/2} E(t) e^{j\omega_0 t} dt \\ + (1 + R) \sum_{\forall n \neq 0} N(\omega_n) Y_n^{(2)} \int_{-T_s/2}^{T_s/2} E(t) e^{j\omega_n t} dt. \end{aligned} \quad (21)$$

The former expression is valid as long as the input and output media are identical. Comparing the integrals in Eq. (21) and rearranging terms, the reflection coefficient is finally expressed in the following way:

$$R = \frac{Y_0^{(1)} - Y_0^{(2)} - \sum_{\forall n \neq 0} |N(\omega_n)|^2 (Y_n^{(1)} + Y_n^{(2)})}{Y_0^{(1)} + Y_0^{(2)} + \sum_{\forall n \neq 0} |N(\omega_n)|^2 (Y_n^{(1)} + Y_n^{(2)})}, \quad (22)$$

where we can identify each of the admittances taking part on the expression as individual transmission lines with

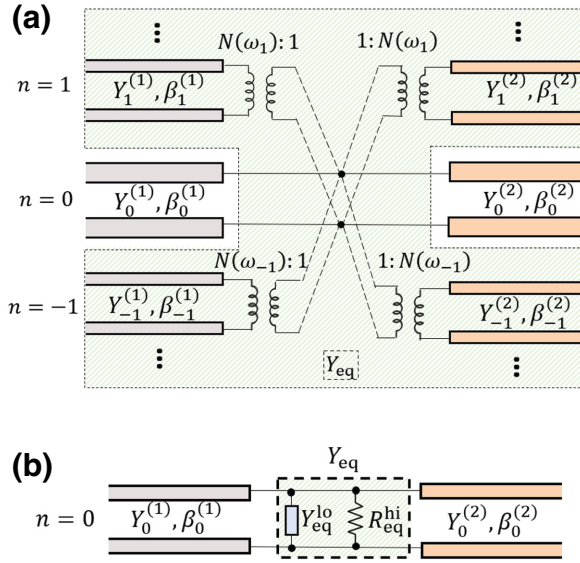


FIG. 3. (a) The equivalent circuit that models the time-modulated metallic screen. It consists of an infinite parallel connection of transmission lines, each representing a different harmonic. (b) The compact equivalent circuit. The equivalent admittance Y_{eq} , which contains all relevant information about the time-varying screen, can be subdivided into low-order (lo) and higher-order (hi) contributions.

characteristic admittance $Y_n^{(i)}$ and propagation constant $\beta_n^{(i)}$. Similar to Refs. [36,42], Eq. (22) is interpreted in circuitual terms by the topology shown in Fig. 3. Each of the parameters $N(\omega_n)$ is interpreted as a complex transformer (it transforms both amplitude and phase). Moreover, the infinite sum in Eq. (22) groups all relevant information about the diffracted waves created by the time-modulated screen. From a circuit standpoint, this term can be interpreted as an equivalent admittance Y_{eq} that reads

$$Y_{\text{eq}} = \sum_{\forall n \neq 0} |N(\omega_n)|^2 (Y_n^{(1)} + Y_n^{(2)}). \quad (23)$$

Thus, the reflection coefficient can be rewritten as

$$R = \frac{Y_0^{(1)} - Y_0^{(2)} - Y_{\text{eq}}}{Y_0^{(1)} + Y_0^{(2)} + Y_{\text{eq}}}. \quad (24)$$

Close inspection of Eqs. (12) and (13) reveals that higher-order harmonics are *propagative* in the present time-modulated screen (for further details, see Appendix A). This can be appreciated by looking at the wave admittances of the n th higher-order mode,

$$Y_n^{(i),\text{TM}} = Y_n^{(i),\text{TE}} \approx \sqrt{\frac{\varepsilon_r^{(i)} \varepsilon_0}{\mu_r^{(i)} \mu_0}} = Y_0^{(i)}, \quad |n| \gg 1, \quad (25)$$

which are real valued (in lossless media), independent of index n , and identical for both TM and TE polarizations.

This suggests that the higher-order modes contribute with a purely resistive term $R_{\text{eq}}^{\text{hi}}$ that can be modeled as a resistor [see Fig. 3(b)]:

$$\frac{1}{R_{\text{eq}}^{\text{hi}}} = (Y_0^{(1)} + Y_0^{(2)}) \sum_{|n| > N_{\text{lo}}} |N(\omega_n)|^2. \quad (26)$$

The minimum n th order associated with a mode participating in Eq. (26), N_{lo} would be calculated by just considering $|\beta_n| \gg k_t$. Thus the summation in Eq. (26) can be calculated once and stored, since it will remain invariant for any incidence angle. The former discussion shows a conceptual change with respect to spatially modulated gratings, where higher-order harmonics are normally evanescent and carry reactive power (capacitive and inductive for TM and TE modes, respectively) [36,37,42].

The situation is different when considering low-order harmonics, the associated wave impedance or admittance of which is a function of, among other parameters, the incident angle θ . Thus, the *complex* low-order contribution of the equivalent admittance present in Fig. 3(b) can be computed as

$$Y_{\text{eq}}^{\text{lo}} = \sum_{\substack{n=-N_{\text{lo}} \\ n \neq 0}}^{n=N_{\text{lo}}} |N(\omega_n)|^2 (Y_n^{(1)} + Y_n^{(2)}). \quad (27)$$

At this point, it is important to remark that an n th TE and TM low-order harmonic now differ. Unlike higher-order harmonics, which behave almost identically regardless of their TM or TE nature [see, e.g., Eq. (25)], admittances associated with lower-order harmonics are governed by the expressions in Eqs. (10) and (11), which exhibit clear differences between them. The global lower-order admittance $Y_{\text{eq}}^{\text{lo}}$ in Eq. (27) varies according to the TE- or TM-incidence scenario, influencing both the reflection coefficient R and the amplitude associated with the lower-order harmonics in both semispaces $E_n^{(1/2)}$. Therefore, the resulting electromagnetic response of the whole system differs with a TE or a TM case in a general oblique-incidence scenario. However, the behavior of the time-varying system is indistinguishable under TE or TM excitation when the incidence is normal to the discontinuity plane (\hat{z} direction according to the frame of coordinates in Fig. 1). TE incidence will just excite TE higher-order harmonics and TM incidence will only excite TM higher-order harmonics. This is typical in 1D problems when the transverse components of the incident wave coincide with \hat{x} and \hat{y} .

D. Diffraction angles

The reflection or transmission angle of each n th-order harmonic is described by

$$\theta_n^{(i)} = \arctan \left(\frac{k_t}{\sqrt{\varepsilon_r^{(i)} \mu_r^{(i)} \left[\frac{\omega_0 + n\omega_s}{c} \right]^2 - k_t^2}} \right). \quad (28)$$

Note that the fundamental harmonic ($n = 0$) is not affected by the time modulation. This implies that the fundamental harmonic simply obeys conventional Snell's law of refraction,

$$\frac{\sin(\theta)}{\sin(\theta_0^{(i)})} = \frac{\sqrt{\varepsilon_r^{(i)} \mu_r^{(i)}}}{\sqrt{\varepsilon_r^{(1)} \mu_r^{(1)}}}, \quad (29)$$

and thus propagates in the same direction of incidence when the considered input and output media are air ($\theta_0^{(i)} = \theta$).

It can be inferred from Eq. (28) that, for the case of normal incidence, $\theta_n^{(i)} = 0, \forall n$. Moreover, the diffraction angle is expected to change inside the dielectric media as $\beta_n^{(i)}$ does. By looking at the expression for $\theta_n^{(i)}$, it can be appreciated that the denser the medium under consideration is, the closer the diffracted angles are to the normal (when the input media is considered to be air). This would be similar to conventional refraction between two media. This phenomenon is even more accentuated if the time-modulated screen commutes rapidly between its two states; namely, if ω_s is large, the diffraction angle for higher-order harmonics goes progressively to zero as $|n|$ increases.

The application of Eq. (28) has important implications from an engineering perspective. Figure 4(a) illustrates a four-dimensional representation of the (normalized) diffraction angle θ_n , assuming that the time-varying screen is surrounded by air. This angle is evaluated as a function of the incident angle θ , the integer index n , and the normalized modulation frequency ω_s/ω_0 ; namely, $\theta_n = \theta_n(\theta, n, \omega_s/\omega_0)$. Only propagative diffraction orders are considered in the figure, while evanescent orders are

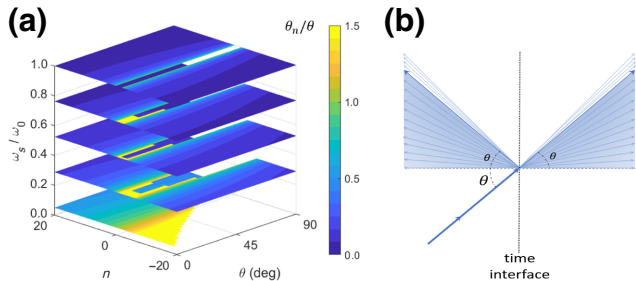


FIG. 4. (a) The normalized diffraction angle (θ_n/θ) as a function of the incident angle θ , the harmonic index n , and the normalized modulation frequency ω_s/ω_0 . Only propagative angles are plotted. Evanescent regions are identified by blank spaces in the figure. (b) A sketch of the diffraction created by the time-modulated interface.

displayed as blank spaces. Note that in the vast majority of scenarios, the normalized diffraction angle is less than the unity; thus θ_n is generally less than θ . Only in cases where $\omega_s \ll \omega_0$ is the diffraction angle θ_n larger than the incident angle θ . Nonetheless, note that if $\omega_s \ll \omega_0$ in Eq. (28), while θ_n will be larger than θ , it will certainly be close to it. On the other hand, the minimum angle at which propagative waves can diffract is $\theta_n = 0$. This is the case for higher-order harmonics ($|n| \gg 1$). Therefore, the range of diffraction angles is limited, in practice, to $\theta_n \approx [0, \theta]$. This situation is conceptually sketched in Fig. 4(b) for an obliquely incident plane wave that impinges on the time-varying interface.

E. Basis-function choice

The choice of the basis function $E(t)$ is crucial to validate the above approach. At this point, it is important to remark that the time period related to appearance or disappearance of the electric wall T_s does not necessarily coincide with the period associated with $E(t)$. In order to make both periods coincide, there must be a particular relationship between ω_s and ω_0 . It can be demonstrated that this relationship must satisfy $\omega_0/\omega_s = p$, with $p \in \mathbb{N}$. Figure 5 illustrates this statement in a visual way. Figure 5(a) represents $E(t)$ for $\omega_0/\omega_s = 1.75$. We observe that $E(t)$ does not repeat within intervals separated by T_s , but within intervals separated by $4T_s$. This situation is not given when $\omega_0/\omega_s = 2$, where the periodicity is exactly T_s , as shown in Fig. 5(b). This last aspect is the situation taken into account in this paper. It is worth remarking that the situation in Fig. 5(a) could also be addressed by considering some additional aspects but is beyond the scope of this work.

The basis function is therefore expressed as follows:

$$\mathbf{E}(t) = \hat{\mathbf{y}} \times \begin{cases} 0, & -T_s/2 \leq t < 0, \\ A \sin(\omega_0 t), & 0 \leq t < T_s/2. \end{cases} \quad (30)$$

When the time-varying screen turns into a *metal* ($-T_s/2 \leq t < 0$), the tangential electric field should

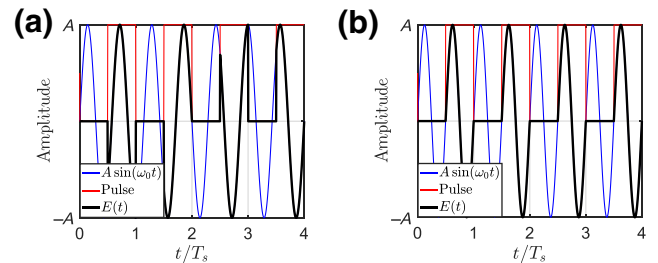


FIG. 5. The field profile $E(t)$ in cases where the time modulation ω_s is slower than the vibration of the incident wave ω_0 : (a) $\omega_0/\omega_s = 1.75$; (b) $\omega_0/\omega_s = 2$.

vanish if a PEC is assumed. When the time-varying screen is in the *air state* ($0 \leq t \leq T_s/2$), the tangential field has the shape of the incident time-harmonic excitation; namely, a sinusoidal wave. Furthermore, the continuity of the electric and magnetic displacement fields \mathbf{D} and \mathbf{B} is guaranteed

at $t = 0$ s, this being strictly mandatory to satisfy the boundary conditions [9].

Computing the Fourier transform to the basis function, we reach the following expression for the transformers in Eq. (19):

$$N(\omega_n) = -\frac{4\omega_0}{\omega_n^2 - \omega_0^2} \frac{e^{-j\omega_n T_s/2} \left[j\omega_n \sin(\omega_0 T_s/2) + \omega_0 \cos(\omega_0 T_s/2) \right] - \omega_0}{j\omega_0 T_s + e^{-j\omega_0 T_s} - 1}. \quad (31)$$

The expressions for the transformers $N(\omega_n)$ gives the relative weight of the harmonics [Eq. (18)]. Note that Eq. (31) indicates that the transformers, and therefore the Floquet harmonics, have a decay $N(\omega_n) \sim 1/n$. This weight is one of the parameters that can be compared to those extracted by FDTD.

Under the above assumption ($\omega_0/\omega_s = p$, with $p \in \mathbb{N}$), it can be appreciated that the reflection and transmission ($T = 1 + R$) coefficients do not depend on time. Both coefficients are the result of the average obtained over the period T_s [see Eqs. (16)–(17)]. In general, this situation is expected to hold as long as the ratio ω_0/ω_s is a rational number. Nonetheless, it should be stated that rational ratios ω_0/ω_s would contain M cycles to form a macroperiod $T = MT_s$, unlike purely integer ratios ω_0/ω_s , the periodic response of which is self-contained in a single period T_s .

Up to this point, we have only considered scenarios where the time modulation is either slower than or identical to the vibration of the incident wave ($\omega_s \leq \omega_0$). Now, Fig. 6 presents some cases where the time modulation is faster than the vibration of the incident wave; namely, $\omega_s > \omega_0$. This scenario is a bit different from the previous ones. It can be demonstrated that the time needed to achieve a complete period is now T_0 instead of T_s , as visualized in Figs. 6(a) and 6(b). This is due to the fact that the period of the incident wave (T_0) is larger than the period of the modulation (T_s) in cases where $\omega_s > \omega_0$. Therefore,

a samplinglike phenomenon arises for the basis function $E(t)$ (black curve), caused by the rapid variation of the screen.

F. Dielectric and magnetic losses

Losses in dielectrics can be accounted for in a straightforward manner. Simply replace the real-valued dielectric constant $\varepsilon_r^{(i)}$ by the complex term [52]:

$$\varepsilon_r^{(i)} \rightarrow \varepsilon_r^{(i)} (1 - j \tan \delta^{(i)}), \quad (32)$$

where $\tan \delta^{(i)}$ is the loss tangent term. A similar rationale can be applied for magnetic losses, where the relative permeability would also be defined by a complex-valued expression. Dielectric and magnetic losses can be incorporated in both models.

III. RESULTS, VALIDATION, AND APPLICATIONS

In order to validate the former approach, some results are presented here. We initially consider the scenario depicted in Fig. 1: a time-modulated metallic screen that periodically vanishes (PEC, $-T_s/2 \leq t \leq 0$; air, $0 \leq t \leq T_s/2$). Initially, both the input and the output media are considered to be air ($\varepsilon_r^{(1)} = \mu_r^{(1)} = \varepsilon_r^{(2)} = \mu_r^{(2)} = 1$). Nonetheless, we should remark that the former approach can be further extended to more complex scenarios involving dielectrics and modulations in both space and time.

Figure 7 illustrates the normalized Floquet coefficients $|E_n|$ extracted using the present approach and a self-implemented FDTD formulation (for specific details related to the FDTD, see Appendix B) for the case of a time-modulated screen with different modulation angular frequencies ω_s . Normal TE incidence is assumed. As an indication, the selected basis function $E(t)$ is also included as an inset in Figs. 7(a)–7(c). Excellent agreement is observed between the results extracted from the Floquet-Bloch approach and the FDTD.

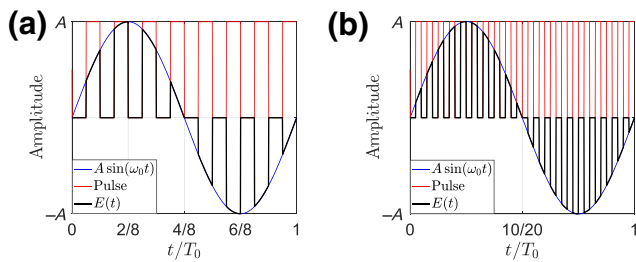


FIG. 6. The field profile $E(t)$ in cases where the time modulation ω_s is faster than the vibration of the incident wave ω_0 : (a) $w_0/w_s = 0.125$; (b) $w_0/w_s = 0.05$.

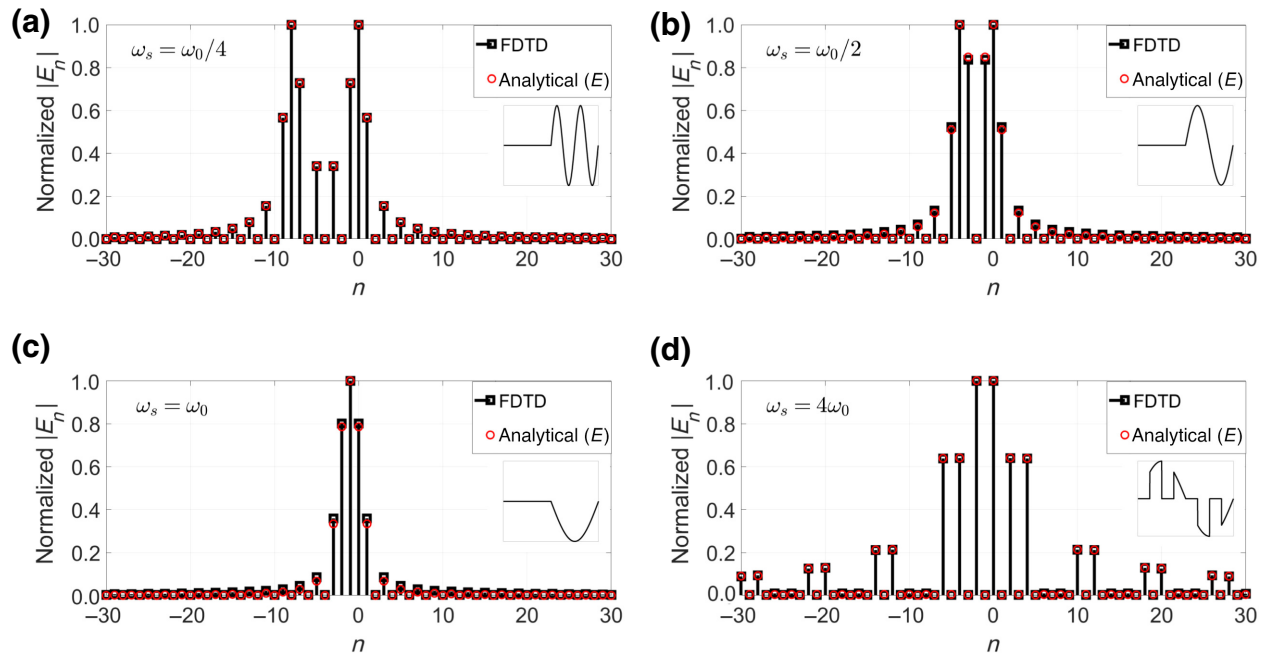


FIG. 7. The normalized Floquet coefficients $|E_n|$ when a TE-polarized plane wave impinges on the time-modulated interface—normal incidence is assumed: (a) $\omega_s = \omega_0/4$; (b) $\omega_s = \omega_0/2$; (c) $\omega_s = \omega_0$; (d) $\omega_s = 4\omega_0$. The analytical results are compared to the FDTD method.

Some conclusions can be drawn by looking at Fig. 7. When the time modulation ω_s is slow compared to the frequency of the incident wave ($\omega_s \ll \omega_0$), the modal separation between the two harmonics that carry the main power contribution is large. This can be appreciated in Fig. 7(a). Conversely, when the time modulation is of the order of the frequency of the incident wave ($\omega_s \sim \omega_0$), then the modal separation between two main harmonics that carry the main power contribution narrows. This is observed in Figs. 7(b) and 7(c). Additionally, it is of interest to note that, in the case $\omega_s = \omega_0$, the harmonic with the highest power contribution is $n = -1$ [see Fig. 7(c)]. This means that a great amount of power could be transferred from the incident wave to (-1) th harmonic, a fact that is of potential interest with regard to exploitation in engineering for beam-forming purposes and the creation of analog mixers [34]. Furthermore, the symmetry of the considered tangential field $E(t)$ causes the higher-order even harmonics to be null, a fact that is corroborated by the FDTD simulation. It is expected that higher-order even harmonics will no longer be null if the times for which the screen is in the air state and in the metal state are not the same; that is, if the change occurs at an instant different from $T_s/2$. Finally, Fig. 7(d) illustrates the amplitude of Floquet harmonics when $\omega_s = 4\omega_0$. Cases where the time modulation is notably faster than the vibration of the incident wave ($\omega_s \gg \omega_0$) suggest that most of the diffracted power transfers to the fundamental ($n = 0$) and $n = -2$ harmonics. According to Eq. (28), both harmonics

have diffraction angles in the same direction of incidence $\theta_0 = \theta_{-2} = \theta$. Moreover, when the screen commutes rapidly, it is expected that a significant amount of power will be transferred to angles close to the normal. This will be verified in further FDTD simulations.

Figure 8 illustrates a FDTD simulation showing the electric field distribution when different time modulations ω_s are considered. In this case, oblique TE incidence ($\theta = 30^\circ$) is assumed. For a better visualization of the diffraction phenomena, only transmitted waves are plotted in this case. The black arrows indicate the theoretical propagation direction of the Floquet harmonics that carry most of the diffracted power. By looking at Fig. 8(a), it can be observed that in those cases where ω_s is much less compared to the frequency of the incident wave ($\omega_s \ll \omega_0$), higher-order harmonics diffract with angles very close to that of the fundamental harmonic $n = 0$. As a consequence, they appear to overlap. This is in agreement with the theoretical expression for the angles of the transmitted waves in Eq. (28). In this scenario, the system acts as a pulsed source of angular frequency ω_s .

Cases where $\omega_s \ll \omega_0$ are not desirable, due to the need to control the steering angle. However, the situation is different when $\omega_s \sim \omega_0$. The fact that the modulation frequency is comparable to the frequency of the incident wave causes the angle of reflection or transmission of higher-order modes to broaden. This is illustrated in Figs. 8(b) and 8(c). Specifically, let us focus on Fig. 8(c), where the time modulation is identical

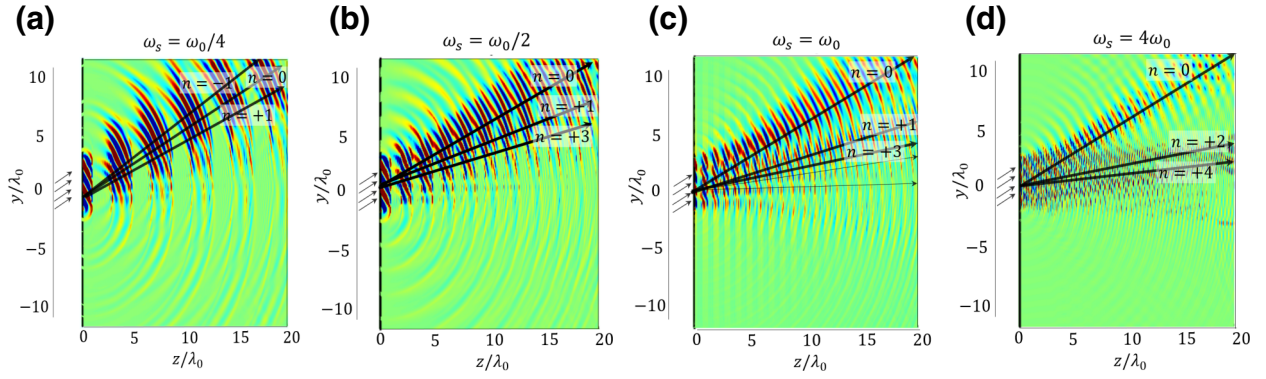


FIG. 8. An FDTD simulation (electric field) showing transmission through a time-modulated metallic screen when a TE-polarized oblique wave ($\theta = 30^\circ$) impinges on the structure: (a) $\omega_s = \omega_0/4$; (b) $\omega_s = \omega_0/2$; (c) $\omega_s = \omega_0$; (d) $\omega_s = 4\omega_0$.

to the frequency of the incident wave. The angle of the transmitted higher-order waves θ_n can be calculated analytically according to Eq. (28). The resulting theoretical values are $\theta_0 = 30^\circ$, $\theta_1 = 14.48^\circ$, $\theta_2 = 9.59^\circ$, and $\theta_3 = 7.18^\circ$. These values are in agreement with the FDTD simulation: $\theta_0^{\text{FDTD}} = \arctan(11.5/20) = 29.89^\circ$, $\theta_1^{\text{FDTD}} = \arctan(5.1/20) = 14.31^\circ$, $\theta_2^{\text{FDTD}} = \arctan(3.4/20) = 9.65^\circ$, and $\theta_3^{\text{FDTD}} = \arctan(2.6/20) = 7.41^\circ$.

As discussed previously, cases $\omega_s \gg \omega_0$ are expected to locate most of the diffracted energy in the direction of incidence ($\theta = 30^\circ$) or relatively close to it. This can be appreciated in the FDTD simulation shown in Fig. 8(d). This can be understood by looking at the sampling that the time-varying screen causes to the incident wave [see Figs. 6(a) and 6(b)]. As the sampling is finer (ω_s increases), the original incident wave is reproduced in a better way. Therefore, the basis function (field profile) $E(t)$ progressively turns into a discrete version of $\sin(\omega_0 t)$, sampled at integer multiples of T_s . Thus most of the power is carried by the harmonics $n = 0$ and $n = -2$, which are electromagnetically identical ($|k_0| = |k_{-2}|$). The remaining diffraction orders transmit and reflect at angles close to the normal and with lower (generally much lower) amplitudes. The comparison between the analytical and FDTD diffracted angles in Figure 8(d) shows good agreement. The analytical values are $\theta_0 = 30^\circ$, $\theta_2 = 9.59^\circ$, and $\theta_4 = 5.74^\circ$, while the values obtained by FDTD are $\theta_0^{\text{FDTD}} = \arctan(11.3/20) = 29.46^\circ$, $\theta_2^{\text{FDTD}} = \arctan(3.5/20) = 9.93^\circ$, and $\theta_4^{\text{FDTD}} = \arctan(2/20) = 5.71^\circ$. In addition, the small amount of transmission observed at angles below 0° is due to numerical noise and should not be confused with waves actually propagating.

Now, Fig. 9 presents a more general FDTD scenario involving reflected and transmitted waves. In this case, the time-varying screen is located at position $z = 20\lambda_0$ and the incident angle is $\theta = 30^\circ$. Following the previous discussion, slow time modulations ($\omega_s \ll \omega_0$) suggest that the time-varying screen acts as a pulsed source, both in reflection and transmission, with virtually null diffraction. This

is sketched in Figs. 9(a) and 9(b). Naturally, the separation between consecutive wave fronts is related to the ratio ω_0/ω_s . Modulations of the kind $\omega_s \sim \omega_0$ [see Fig. 9(c)] show the richest pattern in terms of diffraction, while fast time modulations ($\omega_s \gg \omega_0$) mainly diffract waves in the specular-reflection and direct-transmission angles as well as in regions near the normal [see Figure 9(d)]. Apparently, it can be seen in Figs. 9(a)–9(d) that the amplitude of the reflected waves increases (transmission decreases) as ω_0/ω_s is smaller.

A. Dielectric media

Figure 10 illustrates a FDTD simulation showing the electric field distribution for a structure formed by a time-varying screen backed by a semi-infinite medium of

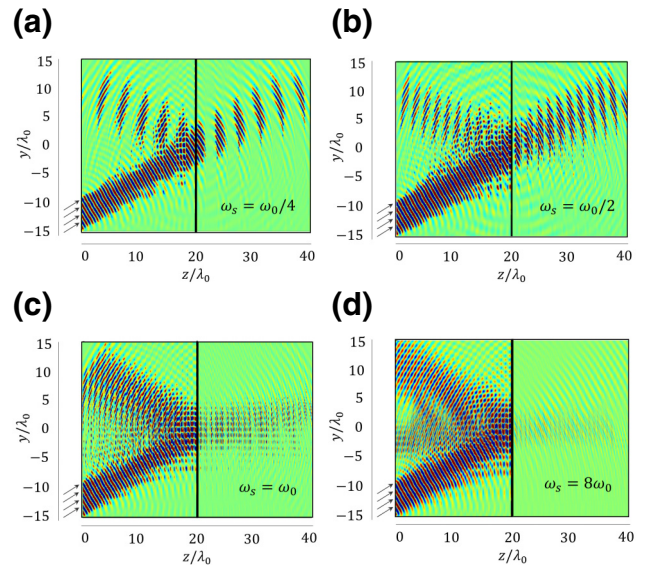


FIG. 9. An FDTD simulation (electric field) showing reflection and transmission through a time-modulated metallic screen when a TE-polarized oblique wave ($\theta = 30^\circ$) impinges the structure: (a) $\omega_s = \omega_0/4$; (b) $\omega_s = \omega_0/2$; (c) $\omega_s = \omega_0$; (d) $\omega_s = 8\omega_0$.

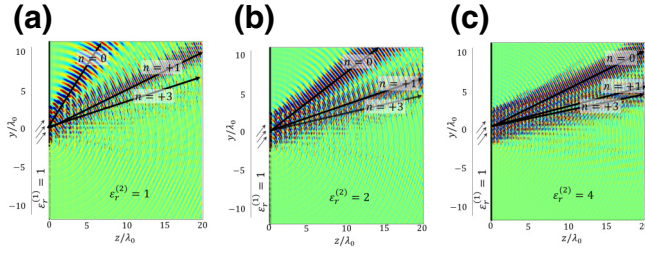


FIG. 10. An FDTD simulation (electric field) showing transmission through a time-modulated metallic screen loaded with a semi-infinite dielectric ε_r when a TE-polarized oblique wave ($\theta = 60^\circ$) impinges the structure: (a) $\varepsilon_r^{(2)} = 1$; (b) $\varepsilon_r^{(2)} = 2$; (c) $\varepsilon_r^{(2)} = 4$. Parameters: $\omega_s = \omega_0$.

relative permittivity $\varepsilon_r^{(2)}$. The input medium is considered to be air and $\omega_s = \omega_0$ to enhance the spacing between angles of different diffraction orders. Then, the angle of transmission of the n th diffracted wave, θ_n , is calculated analytically according to Eq. (28) and compared to the numerical FDTD simulations in Table I. The results show good agreement between the theory and the numerical computations. As already predicted in Sec. IID, large values of $\varepsilon_r^{(2)}$ suggest that the diffracted waves approach to the normal ($\theta = 0$). If the output medium is dense, the higher-order harmonics concentrate on a small angular region close to the normal, which makes them very difficult to visualize in a field chart. As a consequence, diffraction orders $n \geq 3$ are not compared to the FDTD in Table I.

B. Applications

In light of the present results, the applications of the proposed time-periodic metallic screen are directly linked to its diffractive and pulsed-source behavior. In general, diffraction gratings (space-only, time-only, or space-time modulated) are commonly used as filters, monochromators, spectrometers, lasers, wavelength-division multiplexing devices, holographers, polarizers, beam formers, direction-of-arrival (DoA) estimators, and in many other microwave, photonic, and optical applications. Naturally,

TABLE I. The diffraction angle θ_n (degrees) for the n th harmonic in a structure formed by a time-varying screen backed by a semi-infinite medium of relative permittivity $\varepsilon_r^{(2)}$. Parameters: $\omega_s = \omega_0$, $\varepsilon_r^{(1)} = \mu_r^{(1)} = \mu_r^{(2)} = 1$, and $\theta = 60^\circ$.

Diffraction angle (degrees)	θ_0	θ_1	θ_2	θ_3
Theory ($\varepsilon_r^{(2)} = 1$)	60	25.66	16.78	12.50
FDTD ($\varepsilon_r^{(2)} = 1$)	59.40	25.87	16.69	...
Theory ($\varepsilon_r^{(2)} = 2$)	37.76	17.83	11.78	8.81
FDTD ($\varepsilon_r^{(2)} = 2$)	37.48	18.00	11.31	...
Theory ($\varepsilon_r^{(2)} = 4$)	25.66	12.50	8.30	6.21
FDTD ($\varepsilon_r^{(2)} = 4$)	26.10	12.68	8.53	...

gratings can be of reflective or transmissive types, depending on the intended operation. The main advantages of time gratings compared to traditional space gratings are related to the inherent capabilities of time-periodic structures to mix frequencies. This is an inherent property related to the time periodicity, $\omega_n = \omega_0 + n\omega_s$. This fact is a valuable asset that can be exploited in engineering for the design of analog FSS-based mixers.

Furthermore, the combination of time and space periodicities could directly lead to nonreciprocal responses for the considered devices. The search for nonreciprocity has become a hot topic in electromagnetism in recent years, especially if it is achieved by avoiding bulky magnets or, in general, magnetic materials. Next-generation networks based on beam forming can take advantage of the nonreciprocal response of space-time-modulated metamaterials. In fact, the present time-varying screen can efficiently act as a beam former simply by adjusting the frequency modulation ω_s .

On the other hand, pulsed sources are in demand in many fields of physics, engineering, and medicine. For instance, pulsed electromagnetic field therapy (PEMF) uses electromagnetic fields to heal nonunion fractures and other injuries [53]. Spectrometry and spectroscopy are traditional applications of pulsed waves [54]. More exotic applications of pulsed sources can be found in agriculture, where pulsed electromagnetic fields stimulate biological effects of chemically active species in plasma [55]. Time-modulated metamaterials are currently being investigated as a feasible and alternative source of pulsed waves [56]. In fact, the proposed time-varying metamaterial can act as a pulsed source if the modulation frequency is small compared to the vibration of the incident wave ($\omega_s \ll \omega_0$). The wave form of the generated pulses will coincide with the wave form of the incident wave. In this case, the incident wave is a plane wave of sinusoidal nature, so the pulses are also of sinusoidal nature.

In addition, the proposed structure can act as an analog sampler when the modulation frequency is much greater than the vibration of the incident wave ($\omega_s \gg \omega_0$). This phenomenon can be visualized in Fig. 6. The modulation frequency ω_s of the time-periodic screen would control the sampling rate.

IV. CONCLUSIONS

Previous state-of-the-art works have mainly focused on the study of dielectric based metamaterials with spatiotemporal variations. In this work, we present an analytical framework that serves as a basis for the study of time-modulated metal-based metamaterials. The time periodicity of the problem allows us to expand the electromagnetic fields in terms of a Floquet-Bloch series. By imposing continuity of the electric field and an instantaneous Poynting vector across the time interface, the Floquet coefficients,

dispersion curves, and diffraction angles as well as the reflection and transmission coefficients are derived. The present approach comes with an associated equivalent circuit, formed by two input and output transmission lines and an equivalent admittance that models the time-varying screen. This equivalent admittance groups an infinite set of parallel transformers and transmission lines (one per each harmonic). By checking the dispersion curves of the system, we see the linearity (nondispersion) of the modes and the absence of stop bands. In addition, we show that higher-order harmonics are propagative, which is a notable difference compared to spatially modulated diffraction gratings, where higher-order modes are typically evanescent and carry power. Some analytical and numerical (self-implemented FDTD) results are provided in order to validate the approach. The results show that time-modulated metallic screens can act either as pulsed sources (when $\omega_s \ll \omega_0$) or as beam formers (when $\omega_s \sim \omega_0$) to redirect power. Moreover, cases where the time modulation is notably faster compared to the frequency of the incident wave ($\omega_s \gg \omega_0$) suggest that most of the diffracted power is redirected to the fundamental harmonic and to angles close to the normal. These are interesting features that can be considered for the manipulation and reconfiguration of electromagnetic waves in future wireless communications systems.

ACKNOWLEDGMENTS

This work was supported in part by the Spanish Government under Projects No. PID2020-112545RB-C54 and No. RTI2018-102002-A-I00, in part by “Junta de Andalucía” under Projects No. B-TIC-402-UGR18, No. A-TIC-608-UGR20, No. PYC20-RE-012-UGR, and No. P18.RT.4830, and in part by a Leonardo Grant of the BBVA Foundation. We acknowledge the support of the BBVA Foundation for the funds associated with a project belonging to the program Leonardo Grants 2021 for researchers and cultural creators from the BBVA Foundation.

APPENDIX A: HIGHER-ORDER PROPAGATIVE WAVES

The propagation constant in medium (i) reads

$$\beta_n^{(i)} = \sqrt{\varepsilon_r^{(i)} \mu_r^{(i)}} \sqrt{\left[k_0 + n \frac{\omega_s}{c}\right]^2 - [k_0 \sin(\theta)]^2}. \quad (\text{A1})$$

In the case of dealing with higher-order waves ($|n| \gg 1$), $[k_0 + n\omega_s/c]^2 \gg [k_0 \sin(\theta)]^2$ and $|n\omega_s/c| \gg k_0$. As a consequence, Eq. (A1) can be simplified to

$$\beta_n^{(i)} \approx \frac{\sqrt{\varepsilon_r^{(i)} \mu_r^{(i)}}}{c} n\omega_s, \quad |n| \gg 1. \quad (\text{A2})$$

By inserting Eq. (A2) into Eqs. (10) and (11) and noting that $|n\omega_s| \gg \omega_0$ when $|n| \gg 1$, we reach the expression for the wave admittances of higher-order waves:

$$Y_n^{(i),\text{TM}} = Y_n^{(i),\text{TE}} \approx \sqrt{\frac{\varepsilon_r^{(i)} \varepsilon_0}{\mu_r^{(i)} \mu_0}} = Y_0^{(i)}, \quad |n| \gg 1. \quad (\text{A3})$$

As can be appreciated, the TM and TE admittances are identical, real-valued (in lossless media), and independent of n in the case in which we consider higher-order waves.

APPENDIX B: FDTD SIMULATIONS

Numerical simulations are performed with a self-implemented FDTD method programmed in MATLAB. Our FDTD approach is directly derived from Maxwell’s equations by assuming media free of charges and then particularized to 2D cases where the incident plane wave is TE polarized (E_x, H_y, H_z). We work with a staggered FDTD scheme; namely, $\mathbf{H}^{(\Delta t \cdot n)}$ and $\mathbf{E}^{(\Delta t \cdot n/2)}$, where $\Delta t = C\Delta y/c$ is the time step, n is an integer, and C is a dimensionless parameter associated with the Courant-Friedrichs-Lewy (CFL) stability condition. To suppress numerical reflections, second-order Engquist-Majda absorbing boundary conditions are employed. For the simulations, we consider a uniform square grid with spatial resolution $\Delta_y = \Delta_z = \lambda_0/35$ and $C = 0.4$ (for stability: $C < 1/\sqrt{2}$ if $\Delta_y = \Delta_z$). Furthermore, our FDTD approach can include both static [$\varepsilon \equiv \text{ctt}$] and time-modulated dielectrics [$\varepsilon = \varepsilon(t)$]. However, the time-varying metallic screen, located at $z = z_{\text{pos}}$, is directly modeled in our case as a time-dependent boundary condition for the electric field [$E_x(y, z_{\text{pos}}, t) = 0$, for $-T_s/2 \leq t < 0$, $\forall y$]. Additionally, Floquet coefficients can be extracted from the FDTD as part of a postprocessing step. To do so, the tangential electric field $E(t)$, evaluated along the time period at the interface z_{pos} of the screen, should be stored and numerically integrated [see Eq. (17)].

-
- [1] T. Tamir, H. C. Wang, and A. A. Oliner, Wave propagation in sinusoidally stratified dielectric media, *IEEE Trans. Microw. Theory Techn.* **12**, 323 (1964).
 - [2] C. Elachi, Ph.D. Thesis, Division: Engineering and Applied Science, Caltech, 1971.
 - [3] S. Taravati and G. V. Eleftheriades, Generalized Space-Time Periodic Diffraction Gratings: Theory and Applications, *Phys. Rev. Appl.* **12**, 024026 (2019).
 - [4] A. M. Shaltout, A. Kildishev, and V. Shalae, Time-varying metasurfaces and Lorentz on-reciprocity, *Opt. Express* **5**, 246293 (2015).
 - [5] L. Zhang, Z. Q. Chen, S. Liu, Q. Zhang, J. Zhao, J. Y. Dai, G. D. Bai, X. Wan, Q. Cheng, G. Castaldi, V. Galdi, and T. J. Cui, Space-time coding digital metasurfaces, *Nat. Commun.* **9**, 4334 (2018).

- [6] D. M. Solís and N. Engheta, Functional analysis of the polarization response in linear-time varying media: A generalization of Kramer-Kronig relations, *Phys. Rev. B* **103**, 144303 (2018).
- [7] V. Pacheco-Peña and N. Engheta, Temporal equivalence of Brewster angles, *Phys. Rev. B* **104**, 214308 (2021).
- [8] J. Pendry, P. Huidobro, M. Silveirinha, and E. Galiffi, Crossing the light line, *Nanophotonics* **11**, 161 (2022).
- [9] C. Caloz and Z. Deck-Léger, Spacetime metamaterials—Part I: General concepts, *IEEE Trans. Antennas Propag.* **68**, 1569 (2020).
- [10] C. Caloz and Z. Deck-Léger, Spacetime metamaterials—Part II: Theory and applications, *IEEE Trans. Antennas Propag.* **68**, 1583 (2020).
- [11] V. Tiukuvaara, T. J. Smy, and S. Gupta, Floquet analysis of space-time modulated metasurfaces with Lorentz dispersion, *IEEE Trans. Antennas Propag.* **69**, 7667 (2021).
- [12] G. Ptitsyn, M. S. Mirmoosa, and S. A. Tretyakov, Time-modulated meta-atoms, *Phys. Rev. Res.* **1**, 023014 (2019).
- [13] S. Yin, E. Gaffili, and A. Alu, Floquet metamaterials, *eLight* **1**, 1 (2022).
- [14] R. Marqués, F. Martín, and M. Sorolla, *Metamaterials with Negative Parameters: Theory, Design and Microwave Applications*, (John Wiley & Sons, Hoboken, New Jersey, 2008).
- [15] B. A. Munk, *Metamaterials: Critique and Alternatives*, (John Wiley & Sons, Hoboken, New Jersey, 2009).
- [16] A. Alex-Amor, A. Palomares-Caballero, and C. Molero, 3-D metamaterials: Trends on applied designs, computational methods and fabrication techniques, *Electronics* **11**, 410 (2022).
- [17] A. M. Shaltout, V. M. Shalaev, and M. L. Brongersma, Spaciotemporal light control with active metasurfaces, *Science* **364**, 648 (2019).
- [18] Y. Hadad, D. L. Sounas, and A. Alu, Space-time-gradient metasurfaces, *Phys. Rev. B* **92**, 100304 (2015).
- [19] Y. Hadad, J. C. Solic, and A. Alu, Breaking temporal frequencies for emission and absorption, *Proc. Natl. Acad. Sci. (PNAS)* **113**, 3471 (2016).
- [20] D. L. Sounas and A. Alu, Non-reciprocal photonics based on time modulation, *Nat. Photonics* **11**, 774 (2017).
- [21] S. Yin and A. Alu, Efficient phase conjugation in space-time leaky waveguide, *ACS Photonics* **9**, 979 (2022).
- [22] N. Chamanara, S. Taravati, Z.-L. Deck-Léger, and C. Caloz, Optical isolation based on space-time engineered asymmetric photonic band gaps, *Phys. Rev. B* **96**, 155409 (2017).
- [23] M. M. Salary, S. Jafar-Zangani, and A. Mosallaei, Electrically tunable harmonics in time-modulated metasurfaces for wavefront engineering, *New J. Phys.* **20**, 123023 (2018).
- [24] Y. Shi and S. Fang, Dynamic non-reciprocal meta-surfaces with arbitrary phase reconfigurability based on photonics transitions in meta-atoms, *App. Phys. Lett.* **108**, 021110 (2016).
- [25] X. Fang, M. Li, and J. Hang, Accurate direction-of-arrival estimation method based on space-time modulated metasurfaces, TechRxiv Preprint, <https://doi.org/10.36227/techrxiv.17698181.v2> (2022).
- [26] X. Wang and C. Caloz, Spacetime-modulated meta-surface for spacial multiplexing communications, 13th International congress on artificial materials for novel wave phenomena—metamaterials 2019, Rome, Italy, 465–467 (2019).
- [27] T. Itoh, *Numerical Techniques for Microwave and Millimeter-Wave Passive Structures*, (John Wiley & Sons, Hoboken, New Jersey, 1989).
- [28] J. R. Zurita-Sánchez, P. Halevi, and J. C. Cervantes-González, Reflection and transmission of a wave incident on a slab with a time-periodic dielectric function $\epsilon(t)$, *Phys. Rev. A* **79**, 053821 (2021).
- [29] A. Sotoodehfar, M. S. Mirmoosa, and S. A. Tretyakov, Waves in Linear Time-Varying Dielectric Media, 2022 16th European Conference on Antennas and Propagation (EuCAP), Madrid, Spain, 1–5 (2022).
- [30] Z. Wu, C. Scarborough, and A. Grbic, Space-Time Modulated Metasurfaces with Spatial Discretization: Free-Space N -Path Systems, *Phys. Rev. Appl.* **14**, 064060 (2020).
- [31] S. F. Bass, A. M. Palmer, K. R. Schab, K. C. Kerby-Patel, and J. E. Ruyle, Conversion matrix method of moments for time-varying electromagnetic analysis, *IEEE Trans. Antennas Propag.* **70**, 6763 (2022).
- [32] X. Wang, A. Díaz-Rubio, H. Li, S. A. Tretyakov, and A. Alu, Theory and Design of Multifunctional Space-Time Metasurfaces, *Phys. Rev. Appl.* **13**, 044040 (2020).
- [33] M. H. Mostafa, A. Díaz-Rubio, M. S. Mirmoosa, and S. A. Tretyakov, Coherently Time-Varying Metasurfaces, *Phys. Rev. Appl.* **17**, 064048 (2022).
- [34] S. Taravati and G. V. Eleftheriades, Microwave space-time-modulated metasurfaces, *ACS Photonics* **9**, 305 (2022).
- [35] Y. Vahabzadeh, N. Chamanara, and C. Caloz, Generalized sheet transition condition FDTD simulation of metasurface, *IEEE Trans. Antennas Propag.* **66**, 271 (2018).
- [36] R. Rodríguez-Berral, C. Molero, F. Medina, and F. Mesa, Analytical wideband model for strip/slit gratings loaded With dielectric slabs, *IEEE Trans. Microw. Theory Tech.* **60**, 3908 (2012).
- [37] R. Rodríguez-Berral, F. Medina, F. Mesa, and M. García-Vigueras, Quasi-analytical modeling of transmission/reflection in strip/slit gratings loaded with dielectric slabs, *IEEE Trans. Microw. Theory Tech.* **60**, 405 (2012).
- [38] C. Molero, R. Rodríguez-Berral, F. Mesa, and F. Medina, Wideband analytical equivalent circuit for coupled asymmetrical nonaligned slit arrays, *Phys. Rev. E* **95**, 023303 (2017).
- [39] R. Dubrovka, J. Vazquez, C. Parini, and D. Moore, Equivalent circuit method for analysis and synthesis of frequency selective surfaces, *IEE Proceedings—Microw., Antennas Propag.* **153**, 213 (2006).
- [40] R. Rodríguez-Berral, F. Mesa, and F. Medina, Analytical multimodal network approach for 2-D arrays of planar patches/apertures embedded in a layered medium, *IEEE Trans. Antennas Propag.* **63**, 1969 (2015).
- [41] C. Molero, M. García-Vigueras, R. Rodríguez-Berral, F. Mesa, and N. Llombart, Equivalent circuit approach for practical applications of meander-line gratings, *IEEE Antennas Wireless Propag. Lett.* **16**, 3088 (2017).
- [42] A. Alex-Amor, F. Mesa, Á. Palomares-Caballero, C. Molero, and P. Padilla, Exploring the potential of the multi-modal equivalent circuit approach for stacks of 2-D

- aperture arrays, *IEEE Trans. Antennas Propag.* **69**, 6453 (2021).
- [43] W. Yu, L. Sisi, Y. Haiyan, and L. Jie, Progress in the functional modification of graphene/graphene oxide: A review, *RSC Adv.* **10**, 15328 (2020).
- [44] X. Li and H. Zhu, Two-dimensional MoS₂: Properties, preparation, and applications, *Journal of Materiomics* **1**, 33 (2015).
- [45] A. Laturia, M. L. Van de Put, and W. G. Vandenberghe, Dielectric properties of hexagonal boron nitride and transition metal dichalcogenides: From monolayer to bulk, *npj 2D Mater Appl.* **2**, 6 (2018).
- [46] N. Salazar, C. Marquez, and F. Gamiz, *Synthesis of Graphene and Other Two-Dimensional Materials*, Nanophotonics, 2D Materials for Nanophotonics (Elsevier, Amsterdam, Netherlands, 2021), p. 1.
- [47] N. Mishra, J. Boeckl, N. Motta, and F. Iacopi, Graphene growth on silicon carbide: A review, *Phys. Status Solidi A* **213**, 2277 (2016).
- [48] C. Molero, A. Palomares-Caballero, A. Alex-Amor, I. Parellada-Serrano, F. Gamiz, P. Padilla, and J. F. Valenzuela-Valdes, Metamaterial-based reconfigurable intelligent surface: 3D meta-atoms controlled by graphene structures, *IEEE Commun. Mag.* **59**, 42 (2021).
- [49] M. J. Allen, V. C. Tung, and R. B. Kaner, Honeycomb carbon: A review of graphene, *Chem. Rev.* **110**, 132 (2010).
- [50] S.-E. Zhu, S. Yuan, and G. C. A. M. Janssen, Optical transmittance of multilayer graphene, *Europhys. Lett.* **108**, 17007 (2014).
- [51] Q. Hu, J. Zhao, K. Chen, K. Qu, W. Yang, J. Zhao, T. Jiang, and Y. Feng, An intelligent programmable omni-metasurface, *Laser Photon. Rev.* **16**, 2100718 (2022).
- [52] C. Molero, A. Alex-Amor, F. Mesa, Á. Palomares-Caballero, and P. Padilla, Cross-polarization control in FSSs by means of an equivalent circuit approach, *IEEE Access* **9**, 99513 (2021).
- [53] M. S. Markov, Expanding use of pulsed electromagnetic field therapies, *Electromagn. Biol. Med.* **26**, 257 (2007).
- [54] A. Dolla, Pulsed and continuous-wave magnetic resonance spectroscopy using a low-cost software-defined radio, *AIP. Adv.* **9**, 115110 (2019).
- [55] K. Takaki, K. Takahashi, N. Hayashi, D. Wang, and T. Ohshima, Pulsed power applications for agriculture and food processing, *Rev. Mod. Plasma Phys.* **5**, 12 (2021).
- [56] C. Rizza, G. Castaldi, and V. Galdi, Short-Pulsed Metamaterials, *Phys. Rev. Lett.* **128**, 257402 (2022).